Tribology International 189 (2023) 108983

Contents lists available at ScienceDirect

Tribology International

journal homepage: www.elsevier.com/locate/triboint

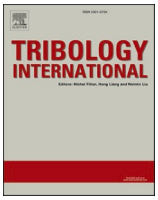

# Effect of peak power on microstructure, mechanical and tribological properties of W-Ti-C-N(O) ceramic films produced by hybrid sputtering

S.A. Ataie [a], M. Soltanieh [a,*], R. Naghizadeh [a], A. Cavaleiro [b,c], F. Fernandes [b,d], F. Ferreira [b,c]

[a] Iran University of Science and Technology, School of Metallurgy and Materials Engineering, Narmak, Tehran 16846–13114, Iran
[b] University of Coimbra, CEMMPRE - Centre for Mechanical Engineering Materials and Processes, Department of Mechanical Engineering, Rua Luís Reis Santos, 3030–788 Coimbra, Portugal
[c] LED&Mat-IPN, Instituto Pedro Nunes, Laboratório de Ensaios Desgaste e Materiais, Rua Pedro Nunes, 3030–199 Coimbra, Portugal
[d] ISEP-School of Engineering, Polytechnic of Porto, Rua Dr. António Bernardino de Almeida 431, 4200–072 Porto, Portugal

ARTICLE INFO

*Keywords:*
Coating
Topography
Indentation
Scratch

ABSTRACT

This research investigates the impact of peak power (from 44 to 105 kW) on the structural and tribological properties of W-Ti-C-N(O) films. Chemical analysis of the coatings, using energy-dispersive spectroscopy and Raman spectroscopy, indicates that increasing target power results in a rise in the oxygen (from 2.6 to 12.0 at%), carbon (from 19.7 to 32.4 at%), and $sp^3$ (from 9.8% to 24.3%) content. Morphological and topographical analysis reveal that an increase in target power causes a transition from a columnar structure (with nodular grains) to a dense structure (with textured grains). The indentation and dry sliding tests demonstrate that the maximum level of $H/E^2$ (0.00047 $GPa^{-1}$) is achieved, along with a low wear rate of 8.1 $\times$ $10^{-7}$ $mm^3$/N.m.

## 1. Introduction

Metallic parts used in cutters, gears, shafts, and blades across various industries, including machining, automobile manufacturing, and turbines, are often subjected to severe stresses under service conditions. This can lead to significant damage due to wear and erosion mechanisms, ultimately reducing the lifespan of the workpiece. To combat these phenomena, it is crucial to improve the surface characteristics of metallic components by utilizing treatments such as depositing hard coatings, with ceramics being preferred due to their low wear rates [1–4]. It has been extensively discussed that depositing ceramic/composite thin films can significantly enhance mechanical properties, provided that the conditions for high uniformity and adhesion to the substrate are met [5–7]. Furthermore, it is essential that the applied thin films exhibit high hardness and thermal stability to withstand sliding or contacting stresses, as higher hardness is necessary in tribology to withstand high loads and stresses [8]. Additionally, due to continuous machining and high temperatures at the contact area (also known as thermal contact [9]), lower thermal conductivity can be desirable to increase the lifespan of mechanical parts. Therefore, employing ceramic materials can be the first choice to meet these requirements [10,11].

Depending on the intended application of the coating (decorative or machining industries), there are some processes (like chemical vapor deposition, arc evaporation and sputtering) to synthesize ceramic films with different microstructures (like multi-layer and composite design) and mechanical properties. For instance, in the decorative industry, a high deposition rate is required and achieving a coating with high uniformity, nano-sized structure, and high toughness is not critical. Reactive sputtering is often considered a promising method for producing smooth thin films without macro-pores and agglomerated particles. Generally, this technique is more prevalent than the aforementioned processes because it can yield defect-free, nano-sized microstructures [12–18]. However, due to low particle energy and diffusion, conventional sputtering (such as direct current magnetron sputtering or DCMS) typically results in a non-uniform surface, with roughness greater than 20 nm [19]. To address this issue and improve thin film uniformity, a new setup called high power impulse magnetron sputtering (HiPIMS) has been developed to enhance particle energy. However, it should be noted that this mode has a significant limitation in that the deposition rate is low [20–22]. The low deposition rate of this process can be attributed to multiple factors. Some important factors include self-sputtering, adatom re-evaporation, and the presence of a dense plasma (which can impede the passage of species involved in the deposition process). The level of target peak power, on-time pulse value of the target and reactive gas flow rate, contribute to the occurrence of

* Corresponding author.
*E-mail address:* mansour_soltanieh@iust.ac.ir (M. Soltanieh).

https://doi.org/10.1016/j.triboint.2023.108983
Received 5 August 2023; Received in revised form 16 September 2023; Accepted 25 September 2023
Available online 26 September 2023

the abovementioned factors [23,24]. To overcome these challenges and produce multi-element thin films simultaneously, it is suggested to use a dual-source chamber (DCMS + HiPIMS) [25,26]. Hybrid sputtering (DCMS + HiPIMS) can ensure a high nucleation rate, ion bombardment, and species diffusion, making it possible to produce a dense and ultra-smooth surface [27]. Moreover, there are deposition parameters (like substrate temperature, substrate bias voltage, gas type/pressure and peak power [19,28–30]) which have a great effect on the microstructure of thin films. Previously, the authors investigated the effect of substrate bias voltage on the mechanical properties of ceramic coatings [31]. However, the effect of peak power in hybrid reactive sputtering (DCMS + HiPIMS) on tribological properties of multi-component thin films has not been published effectively.

Ceramic coatings have become increasingly prevalent in various applications due to their inertness and stability. Transition metal-nitride/carbide (TM-N/TM-C) films can be used in machining and functional surfaces [32–34]. Because of ionic/covalent bonding in ceramic materials, hardness is high, which is desirable for machining performance. Depending on the non-metal element type (N/C/O) and its level (minor levels can be regarded as an impurity and major levels can be regarded as a principal component), thin film microstructure and properties can be altered absolutely [4,35–37]. Additionally, Ti/W-N and Ti/W-C thin films are suitable candidates for obtaining wear-resistance surfaces [34,38–40]. Furthermore, to gain higher hardness, toughness and thermal stability, a new class of materials called medium/high entropy alloys (also named complex alloys which are composed of more than three elements) has been employed recently [11,28,41]. Studying the mechanical properties of carbonitride systems, such as W-Ti-C-N, illustrated that this system can be a promising candidate for protecting WC and steel surfaces [19,31,42–44]. Further, some papers [45,46] have investigated the mechanical properties of M1-M2-M3-C-O or M1-M2-M3-M4-M5-O-N (where Mi is a metallic element) systems. To add to it, there are some works [47–49] that focus on producing Ti-C-N-O thin films and one paper [50] studied the mechanical properties of Ti-Ca/Zr-C-N-O thin films for biological application. Unfortunately, these old articles [47–50] did not scrutinize film chemistry (especially the origin and role of oxygen in TM-C-N thin film features [51,52]) and morphology to establish significant structural-properties relationships. Nonetheless, the microstructure and tribological characteristics of thin films based on M1-M2-C-N-O system (especially W-Ti-C-N-O system) have not been reported yet. However, strengthening industrial surfaces with ceramic coatings has a major disadvantage due to their brittle nature. Thus, to gain wear-resistant thin film, it is necessary to design the structures with maximum substrate-coating adhesion (for example, by employing transition layers) and toughness [53–55]. Also, there is significant interest in synthesizing hard and frictionless coatings, such as amorphous and diamond-like carbon (DLC) phases [49,56,57].

The main objective of this paper is to study the impact of HiPIMS peak power levels on the chemistry and morphology of W-Ti-C-N(O) thin films. Subsequently, the mechanical properties (hardness and toughness) will be analyzed using indentation methods, and tribological behavior (adhesion and friction) will be examined through scratch and pin-on-disk tests. Finally, the study will also investigate the effect of a high concentration of carbon and oxygen in thin film properties.

## 2. Materials and methods

### 2.1. Deposition conditions

To produce W-Ti-C-N(O) thin films, a titanium target (99.99%) was attached to the HiPIMS source (Cyprium™ plasma generator, Zpulser Inc.), while a tungsten carbide target (99.95%) was connected to the DCMS source (Hüttinger PFG 7500 DC). Both targets had dimensions of 150 × 150 × 10 mm, and the distance between the target and substrate was 80 mm. Silicon [100] wafers (15 × 15 mm) and AISI D2 steel workpieces (⌀ 25 × 8 mm) were used as substrates. The silicon wafers covered by thin films were employed in XRD, Raman, SEM, EDS, AFM, and nano-indentation tests, while the steel surfaces covered by coatings were used in scratch and pin-on-disk tests. Prior to deposition, the substrates were cleaned with acetone, distilled water, and ethanol ultrasonic baths. Throughout the deposition process, the substrates were mounted on an aluminum holder which rotated at a speed of 23.5 revolutions per minute around the central axis of the deposition chamber. The base pressure was set at $3 \times 10^{-4}$ Pa before each deposition, and the substrates were not heated. In the HiPIMS process, it is uncommon to heat the substrates since the species involved in the process possess sufficient energy. During the depositions, nitrogen ($N_2$) was used as the reactive gas, while argon (Ar) was used as the plasma gas. Then, a layer of Ti+ TiN ($N_2$/Ar is 0.5) was deposited before the main runs. The deposition time for this layer was 16 min. The nitrogen gas used had a purity level of 99.99%, while the argon gas used had a degree of purity of 99.999%. Unfortunately, these purity levels were not the maximum achievable (99.9999%), and it is possible for oxygen to enter the sputtering chamber. The oscillation duration, maximum on-time, and oscillation period of the voltage-current diagrams were 1800 μs, 6 μs, and 70 μs, respectively. Table 1 shows the deposition parameters. By increasing the target power step by step, five samples were obtained with designations of P44, P59, P89, P105, and P120. However, samples P59 and P120 are not discussed in the following sections. Sample P59 was characterized in a previous study [31], and its characteristics are similar to the first sample (P44). Additionally, sample P120 had a low deposition rate, poor surface smoothness, and inferior mechanical properties (see Fig. S1 in the supplementary file). The thickness of P59 was 1.07 μm and the thickness of P120 was 0.7 μm. To ensure consistent conditions for each analysis, it is preferable to maintain a uniform coating thickness across all samples. This approach helps to minimize any potential variations that could arise from differing coating thicknesses. However, in this particular case, it may not be applicable to apply the approach. On one hand, as stated in the introduction, the deposition rate can be influenced by the peak power. On the other hand, extending the total deposition time for certain samples (to have identical thicknesses) can have detrimental effects. There are two main reasons for this. Firstly, there is an increased likelihood of arcing [58], which can occur during prolonged deposition times. Secondly, a longer deposition time can lead to a higher influx of impurities into the chamber, resulting in a higher level of contaminants in the coatings. Moreover, reducing the deposition time (in order to achieve identical thicknesses) is not advisable since it is preferable to have coating thicknesses exceeding 0.8 μm for tribological applications. Therefore, it is recommended to maintain a fixed deposition time and investigate the hybrid sputtering behavior. This approach will allow for the identification of conditions that yield both maximum deposition rate and favorable mechanical responses simultaneously.

### 2.2. Characterization methods

The surface and cross-sectional morphology of W-Ti-C-N(O) thin films were studied by Quanta 400FEG-SEM. The applied electron beam was fixed at 5 keV and a secondary electron detector was employed for imaging. Energy Dispersive Spectroscopy with ZAF (atomic number-Z-, absorbance-A-, and fluorescence-F-) corrections was used to measure

**Table 1**
Deposition parameters.

| Parameter | Level |
|---|---|
| Total time | 120 min |
| Substrate bias voltage | -40 V |
| $N_2$ flow rate | 7 sccm |
| Ar flow rate | 14 sccm |
| Peak power | 44, 59, 89, 105, 120 kW |

elemental compositions. To reduce errors, five different locations of thin films were analyzed and the average is reported. Geometrical features of coating surfaces were investigated by atomic force microscopy (Bruker Innova). Gwyddion software (v. 2.60) was employed to analyze AFM images and extract fractal parameters. Ra (average roughness), Rq (root mean square roughness), Sk (skewness) and Ku (kurtosis) were introduced in the previous papers [28,59]. The phase structure of the films was investigated by X-ray diffraction (grazing incidence mode with the angle of 1°) and Raman spectroscopy. The XRD set-up was Analytical X'Pert PRO MPD with Cu radiation (45 kV and 40 mA-$\lambda = 1.54$ Å) and the Raman spectroscopy was Renishaw with a He-Cd laser of 325 nm ($\lambda$ is 325 nm).

Indentation is a suitable method for extracting the hardness, Young's modulus (based on the Oliver and Pharr method [60]), and deformation/fracture behavior [61] of various surfaces. A nano-indentation tester (Micromaterials Nano Tester) with a Berkovich diamond tip was used to determine the hardness and Young's modulus of the coatings. The load was fixed at 10 mN and the indentation process was repeated sixteen times to take the average value. In addition, high-load indentations (100 mN, 450 mN and 1000 mN with Vickers tip) were employed to see the coating toughness and fracture behavior. A scratch set-up (CSEM – REVETEST) with Rockwell "C" diamond-tip (∅ 200 μm) was used to evaluate substrate-thin film adhesion (speed was 10 mm/min and loading was varied from 0 to 60 N). The wear behavior of the layers was measured by pin-on-disk method (homemade set-up) at room temperature (23 °C) and humidity (40%). The counterpart was AISI 52100 ball (∅ 10 mm and the length was 40 mm). The load content and rate were fixed at 5 N and 0.1 m/s. The sliding motion was performed in the absence of lubrication. The wear radius, measured from the center, was 7.6 mm. The pin-on-disk tests were applied three times on each sample, and the average data is presented for the friction coefficient and wear rate. For each sample, the wear rate was calculated using the formula $k = V / (S \cdot L)$, where V represents the volume of mass loss, S denotes the sliding distance, and L represents the constant load. The wear rate is expressed in units of $mm^3$ /N.m. The value of V can be determined through two methods: either by measuring the mass loss directly or by utilizing 2D wear track profiles. Due to the drawbacks associated with the first method (mass measurement), the second method, which involves graphical analysis with the assistance of Autodesk AutoCAD (version 2022), was chosen as the preferred approach for determining the volume of mass loss. For each sample, based on the 2D wear track profile (Fig. 1a), the worn volume was calculated (Fig. 1b). Additionally, it should be noted that the wear characteristics for the 2000-cycle duration are reported for each sample. In the case of the friction coefficient graph for each sample, fluctuations may be observed due to the fact that it represents the average of three runs. In the case of the friction coefficient value for each sample, the initial data below 200 and 280 cycles were excluded due to the running-in phenomenon of P44 and the others, respectively. Subsequently, the average value was calculated from the remaining data.

## 3. Results

### 3.1. Microstructure of the coatings

#### 3.1.1. Chemical analysis

The elemental percentages of the W-Ti-C-N(O) coatings, as determined by EDS analysis, are presented in Table 2. These data were taken from the coating surface, and EDS data are shown in the supplementary file (see Fig. S2 and S3). It can be observed that increasing the target power (from 44 to 105 kW) can result in a significant decrease in the metallic components (tungsten and titanium). Moreover, it is interesting to note that the oxygen content in samples P89 and P105 increased significantly (by more than 8 at%), despite the absence of an oxygen source (the reactive gas was not oxygen, and the targets did not sinter with oxide compounds, as described in reference [50]). Generally, oxygen can enter thin films during deposition (due to dust and inadequate vacuum conditions [6]) or after deposition (via residual gas in the chamber and ambient air) [51,52]. It is possible that the high oxygen percentage in P89 and P105 is related to the purity of the gases in the chamber. As mentioned before, the purity of nitrogen and argon sources was not as high as recommended (99.9999%). Typically, oxygen serves as an impurity constituent during the synthesis of carbonitride thin films, and its content is below 6 at% [19,31]. However, if the oxygen level is high enough (as in samples P89 and P105), then this element should be regarded as a principal component in the thin films (W-Ti-C-N-O), unlike sample P44 (W-Ti-C-N). Similar results were reported in another study [46]. Also, it must be mentioned that carbon and carbon-to-nitrogen ratio increases considerably with increasing target power. To study phase contributions in W-Ti-C-N(O) thin films, grazing incidence XRDs are shown in Fig. 2. As can be seen, peak intensities in sample P44 are low and in samples P89 and P105 are extremely low. Hence, the phase structure has a composite mode with an amorphous phase (which is major) and low content of crystalline phases (which are minor). Furthermore, the peaks located at 36.2̊, 38̊, 42.5̊ and 61.7̊ are broad for a couple of reasons. Firstly, it must be noted that the crystalline phases synthesized during sputtering deposition mostly tend to have a nano-sized nature. Secondly, it may be attributed to the pattern

**Table 2**
Elemental percentage of thin films based on EDS analysis.

| Sample code | W [at%] | Ti [at%] | N [at%] | C [at%] | O [at%] |
|---|---|---|---|---|---|
| P44 | 18.2 | 14.8 | 44.6 | 19.7 | 2.6 |
| P89 | 13.6 | 12.8 | 34.6 | 26.9 | 12.0 |
| P105 | 13.4 | 11.6 | 33.8 | 32.4 | 8.8 |

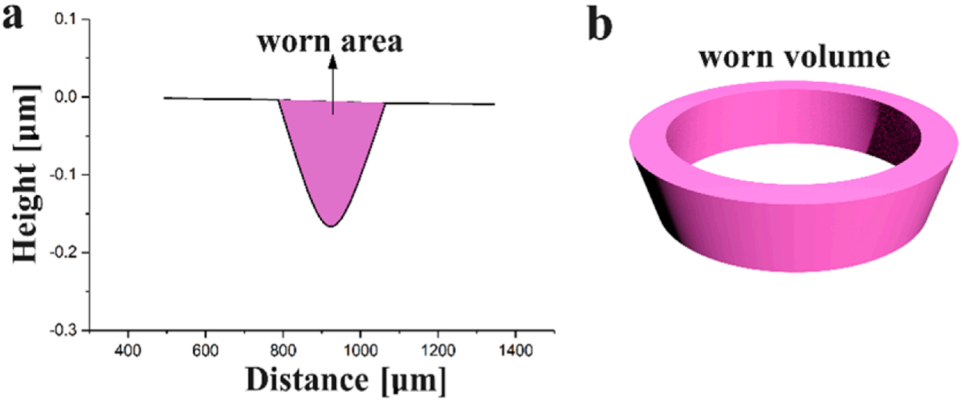


**Fig. 1.** Schematic representing a 2D wear profile (a) and 3D worn volume (b).

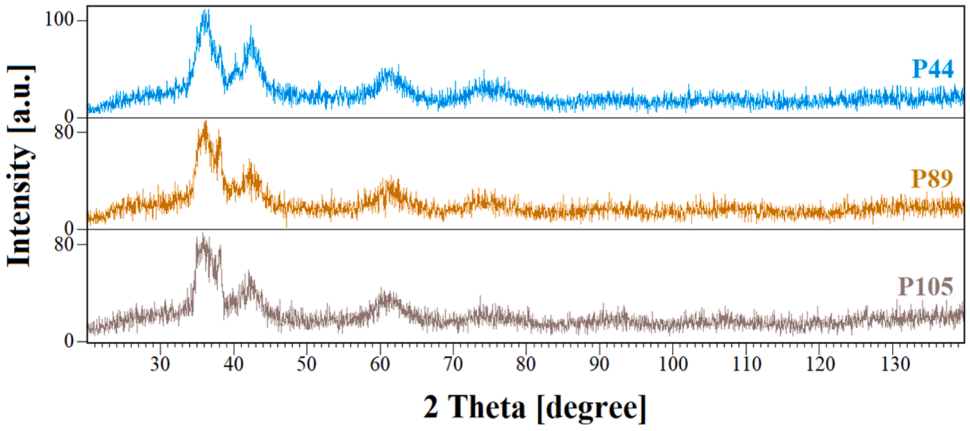


**Fig. 2.** grazing incidence XRD of thin films.

overlapping of various phases in low amounts (some carbide/nitride/-oxide peak positions are similar). These peaks can be assigned to tungsten carbides (WC with Ref. Code= 01–073–0471 and $WC_{1-x}$ with Ref. Code= 00–020–1316), tungsten nitrides (WN with Ref. Code= 96–153–8665 and $W_2N$ with Ref. Code= 00–025–1257), titanium carbide (TiC with Ref. Code= 96–591–0092), titanium nitride (TiN with Ref. Code= 00–038–1420), titanium oxide ($TiO_2$ with Ref. code=96–900–4138) and titanium carbonitride ($TiC_{0.2}N_{0.8}$ with Ref. Code= 01–076–2484). As a consequence, XRD results cannot clearly analyze the phase structure of this system, and another method of evaluation has to be involved.

According to Constable's works [62,63], Raman analysis with

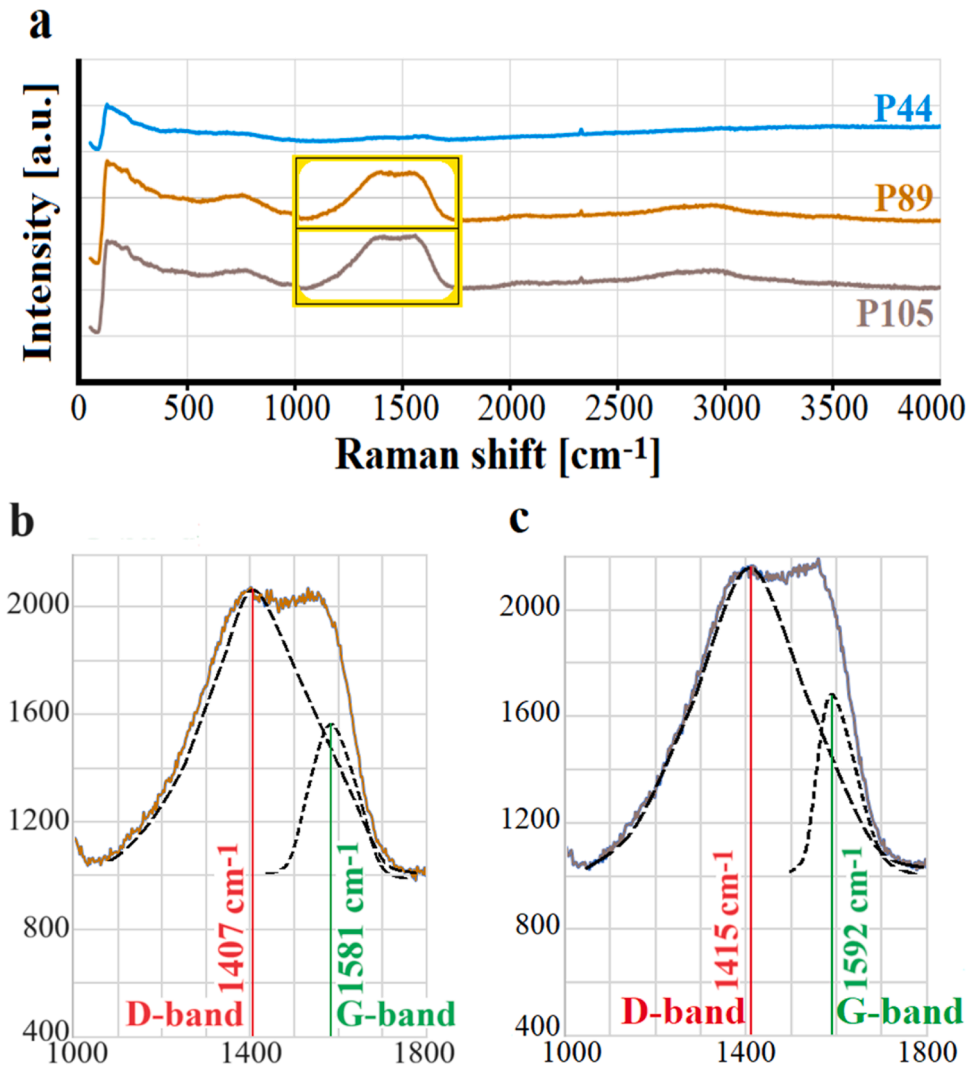


**Fig. 3.** (a) Raman spectra of thin films, (b and c) high magnification of the yellow-black insets in (a) with Gaussian curves of P89 and P105, respectively (for interpretation of the references to color in this figure legend, the reader is referred to the web version of this article.).

suitable wavelengths (compared to the thin film thickness) is an efficient way to reveal bond interactions in protective coatings. Thus, to analyze the bond chemistries of W-Ti-C-N(O) thin films, original and deconvolution curves are presented in Fig. 3. As can be seen from Fig. 3a, it is vivid that there is a difference in the phase structure of sample P44 and samples P89 and P105 in the range of 1000–1800 $cm^{-1}$ (indicated by the yellow insets in Fig. 3a). This range is devoted to free and amorphous carbon [64]. It must be noted that intensities in Fig. 3a were normalized (the intensity of each point divided by 400, where 400 is the difference between the background intensity and the lowest intensity in P44) and there are low carbon peaks in the case of P44. The $I_D$ band can be employed to represent the intensity of disordered carbon, while the $I_G$ band is used to represent graphite carbon. It can be estimated that with increasing peak power, carbon is detached from WC and entered into coatings enormously. The decomposition of the original curves (solid lines of P89 and P105) into Gaussian curves (dashed lines of D and G peaks) is illustrated in Fig. 3b and c. Therefore, it becomes evident that the significant increase in both D-band and G-band intensity can be attributed to the augmentation of peak power and carbon content. To extract the carbon bond strength ($sp^3$: $sp^2$ ratio), full width at half maximum (FWHM) of D/G peaks and intensities ($I_D/I_G$) should be accounted for [57]. In samples P89 and P105, the FWHM of the D shoulder is 273 and 275 $cm^{-1}$ and the FWHM of the G shoulder is 88 and 81 $cm^{-1}$, respectively. Hence, the trend is not clear. But, according to the marker lines of D and G bands (red and green lines in Fig. 3b and c), it is noteworthy to note that the value of $I_D/I_G$ of P44, P89 and P105 is 1.42, 1.35 and 1.27, respectively. This parameter is inversely proportional to the $sp^3$ content [65,66]. Further, it must be pointed out that increasing peak power can cause a right shift in the D and G band positions. The D-position of P89 is 1407 $cm^{-1}$, while it is located at 1415 $cm^{-1}$ for P105. Likewise, the G-position of P89 is 1581 $cm^{-1}$, while it is located at 1592 $cm^{-1}$ for P105. It must be mentioned that the FWHM and G-position of polymer-like carbon (PLC) and graphite-like carbon (GLC) are lower than these results [67]. Therefore, it can be claimed that the phase can be related to the diamond-like carbon (DLC) structure. In addition, vibrational frequencies at 151 $cm^{-1}$ (acoustic phonon mode) and 802 $cm^{-1}$ (optic phonon mode) belong to $W_2N$ and TiCN bonds. These results are in good agreement with other works [38,62]. However, it must be noted that this phase structure (amorphous carbon + $W_2N$ crystalline phase + TiCN crystalline phase) is not complete, and some unknown amorphous phases may exist in the coatings.

### 3.1.2. Morphology

Fig. 4 shows SEM images of the cross-sectional morphology of W-Ti-C-N(O) thin films. As the deposition time is equal for three samples and the thicknesses decrease continuously, it can be concluded that increasing target power can cause a remarkable decrease in the deposition rate. This result is in accordance with other works [22,30]. The lower deposition rates observed at high peak powers (P89 and P105) can be attributed to the self-sputtering phenomenon [68]. Moreover, it can be seen that the first sample (P44) gets a columnar feature (highlighted with random yellow pillars in Fig. 4a). As previous studies have indicated [25,26], micro-voids exist abundantly within these pillars (highlighted by a red ellipse). Increasing peak power results in a peculiar rise in oxygen content in the other samples (P89 and P105), which can be detected in Fig. 4b and c. It is evident that the top sections of these coatings are featureless (in the amorphous state) and the bottom sections take the small columns (as they are interlayers). Fig. 5 displays the surface feature of the coatings with top-view SEM images. It is apparent that samples P44 and P89 have nodular grains with minimal size (Fig. 5a and b), while P105 shows textured and larger grains (see Fig. 5c). It is important to note that there are no macro-defects (like macro-voids and agglomerated particles [6]) on the top surface of the films, and uniformity is well achieved. However, to accurately assess the uniformity, the height distribution should be studied carefully.

Fig. 6 indicates the AFM results (segmented mask on 2D AFM picture + height profile) from the surface of each coating. According to Fig. 6a, b and c, it can be seen that surface grains in P44 and P89 are smaller than those in P105. Further, it is quite clear that grains in P44 and P89 are nearly circular but they are elongated in P105 (see red cells in Fig. 6c). This result is consistent with the findings from the electron microscopy images (Fig. 5). The height profiles of W-Ti-C-N(O) films are presented in Fig. 6a′, b′ and c′. To explain more, Gwyddion analyzed AFM images. Thus, the average grain size (d) at the surface of the samples are listed in Table 3. Further, the grain size trend exhibits an extremum. Besides, Gwyddion analyzed the height profiles to investigate roughness numbers (Ra, Rq, Sk, Ku) and the results are written in Table 3. Apparently, one can recognize that with increasing target power, roughness (average or root mean square value) and Kurtosis increase. The increase in surface roughness observed with increasing target power can be attributed to the phenomena of adatom re-evaporation and shadowing [24]. Skewness behaves inversely, and the interesting aspect is that textured grains get a high negative value, which is similar to the previous work of the authors [31].

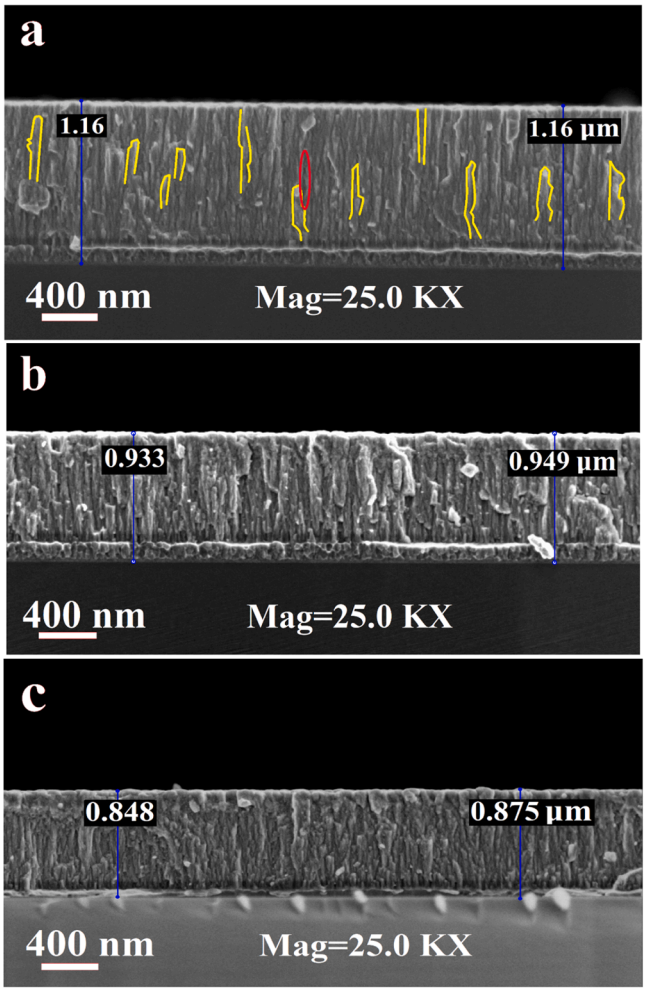


**Fig. 4.** Cross-sectional SEM images of thin films, respectively; (a) P44 with large yellow columns and micro-voids between columns (red ellipse), (b) P89, (c) P105 (for interpretation of the references to color in this figure legend, the reader is referred to the web version of this article.).

### 3.2. Mechanical properties of the coatings

The hardness (H) and elastic (Young's modulus/E) properties of W-Ti-C-N(O) layers based on low load indentation (10 mN) are summarized in Table 4. Higher hardness values are achieved compared to the

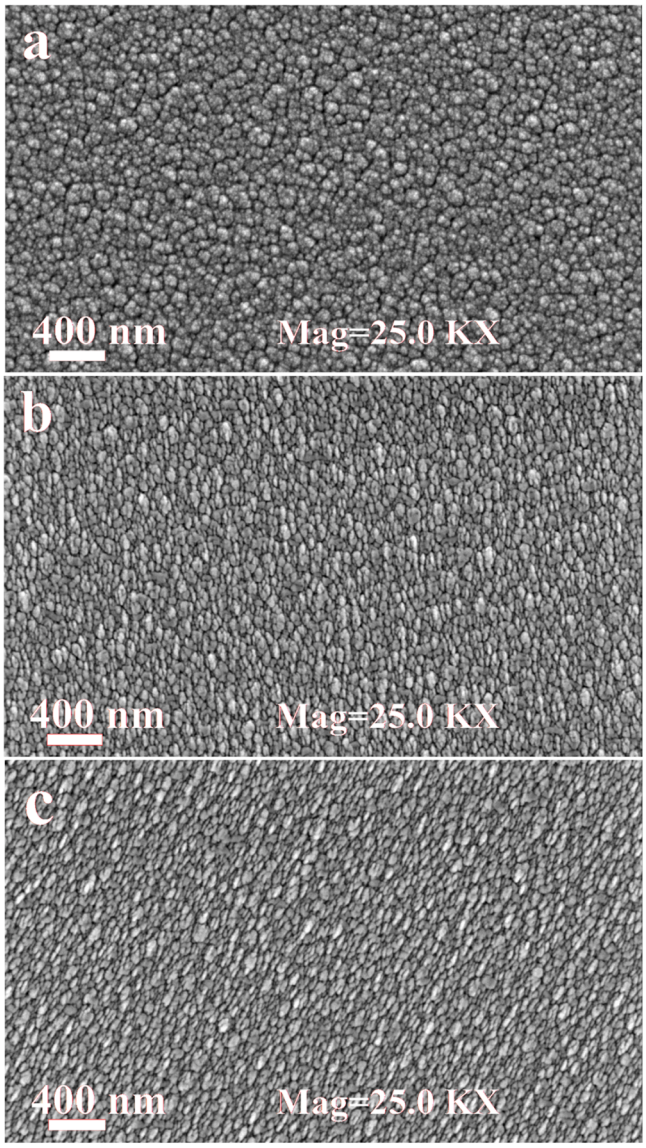


**Fig. 5.** Top-view SEM images of thin films, respectively; (a) P44, (b) P89, (c) P105.

reported data (18.5 GPa) in Ref. [34]. Also, the toughness parameters of the coatings (H/E, $H^3/E^2$ and $H/E^2$ [69]) are presented in Table 4 (load-displacement curves of the samples are presented in Fig. S4 in the supplementary file). In general, like most of the related publications [10,16,36,46,55], it is necessary to trace the trend of H/E and $H^3/E^2$ to check the deformation-resistance value of the surface material. As can be seen from Table 4, when the target power increases, the hardness and toughness parameters (H/E and $H^3/E^2$) will elevate. However, resistance to plastic deformation ($H/E^2$) [70] is more important in ceramic materials because it elucidates the homogenous character of deformation during depth-sensing indentation experiments. Hence, unlike the trends observed for H, H/E and $H^3/E^2$, the trends for elastic modulus and $H/E^2$ show extremums, and P89 represents the minimum Young's modulus and maximum $H/E^2$.

It is suggested that higher loads should be employed to study crack propagation/resistance behavior. Therefore, high load indentations (with 100 mN, 450 mN and 1000 mN) were applied to the W-Ti-C-N(O) thin films. The first thing that can be detected is that under 100 mN loading, there is no signs of cracks and failure (see Fig. S5 in the supplementary file). It is fascinating because some related ceramic coatings [26] cannot bear 50 mN loading, and cracks propagate. By increasing the load (450 mN), some circumferential and radial cracks appear. The deformation area is calculated and written in the center of the contact area in Fig. 7. The second point is that higher loads (1000 mN) can cause buckling and fracture. Crack densities and inhomogeneous deformations are presented in Fig. 8 (for P105) and Fig. S6 (shear bands in P44 and P105) in the supplementary material. These characteristics are listed in Table 5. The created cracks may be attributed to the common mechanisms of shearing and tearing in ceramic films [15]. High load indentations (performed using either the Berkovich or Vickers tip) were conducted five times, and they exhibited similar behavior (e. g., 3 indents in Fig. 8a). Furthermore, the indentations were performed at distances exceeding 30 μm from each other to minimize the influence of neighboring effect. By repeating the indentations at different locations on the sample, the errors associated with indentation measurements can be reduced.

Briefly, static loads alone cannot reveal all the mechanical properties of the surfaces, so dynamic loads (like scratch tests) are useful to inspect coating-substrate adhesion and crack propagation resistance strength [5]. Consequently, three scratch tests were applied on the coatings (see Fig. S7 in the supplementary file). Then two critical loads which indicate the first crack appearance ($L_C1$), delamination starting point ($L_C2$) and crack propagation resistance (CPR as defined by Eq. 1 [54]) are extracted and summarized in Table 5. It is transparent that sample P44 shows the minimum adhesion and CPR. So, to look carefully, a higher magnification of the first stage of its delamination and failure is presented in Fig. 9. Firstly, cracks appeared (red scars in Fig. 9b), and then with increasing loads/stresses buckling, spallation and minor delamination on the scratch sides are created (green and blue insets in Fig. 9b). These observations are in line with older discoveries [5,56]. However, total delamination occurred inside the scratch track (purple arrow in Fig. 9a). It should be noted that increasing peak power can improve adhesion and CPR significantly.

The friction results obtained from pin-on-disk sliding tests on the W-Ti-C-N(O) layers are presented in Fig. 10. The average friction coefficient is nearly the same (0.46±0.05) for all samples. By comparing with previous study [31], it can be inferred that the friction coefficients of the current samples are lower, which can be attributed to the higher amorphous carbon content (which can cause graphitization during sliding) [49]. It should be noted that the friction behavior of the first sample (P44) is not clear because the CoF fluctuation is high (0.18). This behavior (sudden increase and sudden decrease under friction) can lead to significant damage. As a result, the wear width and depth of P44 are high, while they are minimal for P89 (see 2D-wear profiles in Fig. S8 in the supplementary file). Fig. 11 displays the SEM image and oxygen line-EDS analysis of the wear track for each sample. It is evident from the observation that higher oxygen levels within the wear track can be attributed to the oxidative wear mechanism. This finding aligns well with a previous study [31], providing further support and agreement with the obtained results. Furthermore, based on the 2D-wear profiles (Fig. S8 in the supplementary file), it is evident that the wear tracks exhibit a nearly V-shaped morphology. From this result, it can be inferred that ploughing/abrasive wear mechanism may also be dominant in the wear process. Indeed, the columnar morphology and low hardness/toughness parameters of P44 can contribute to a higher wear rate ($2.7 \times 10^{-5}$ $mm^3$/N.m) compared to other samples. On the other hand, P89, with its smooth surface and minimum grain size, tends to exhibit minimum wear rate ($8.1 \times 10^{-7}$ $mm^3$/N.m). A smooth surface can reduce friction and minimize abrasive interactions between the material and pin, resulting in less wear.

$$CPR=LC1(LC2-LC1) \quad (1)$$

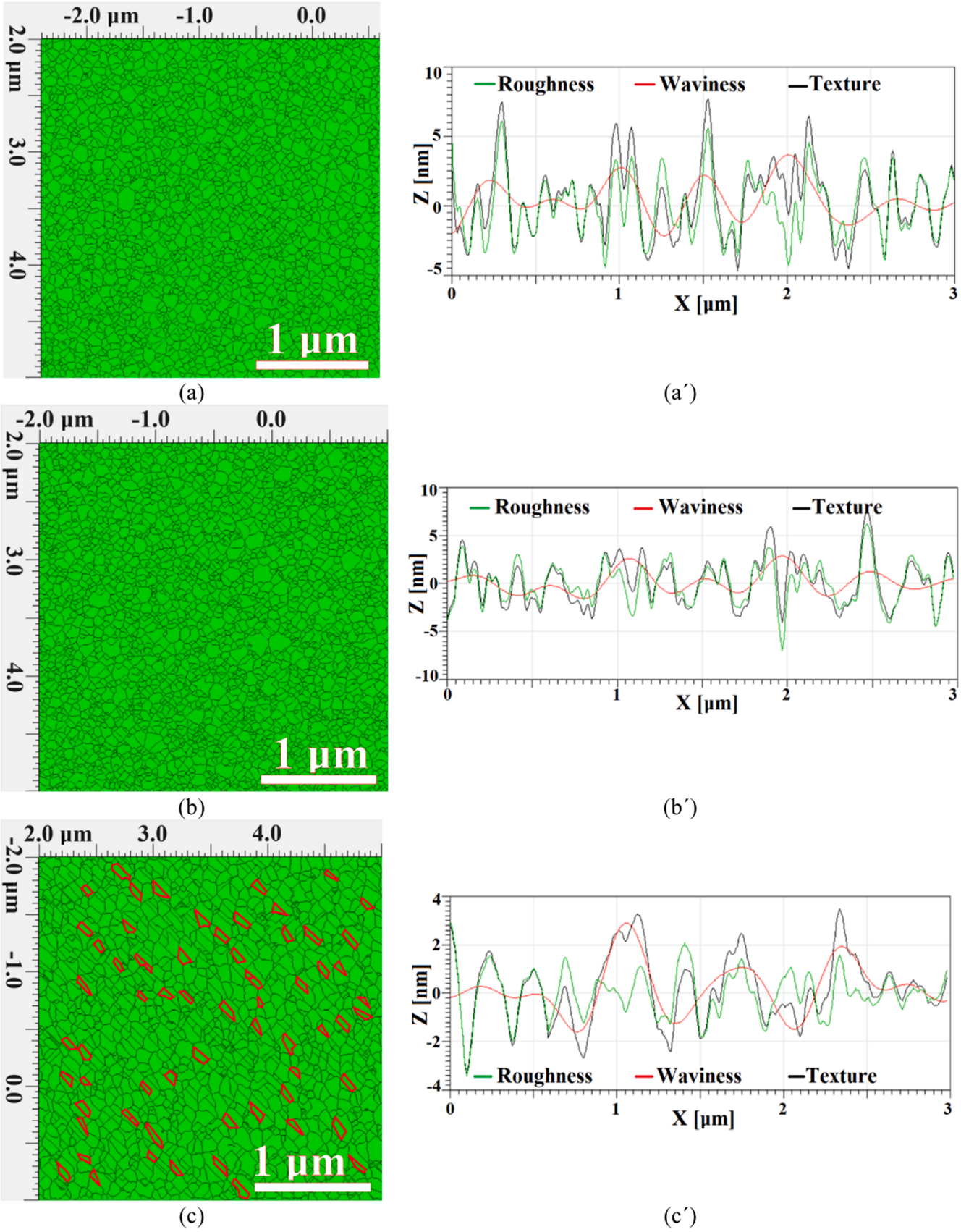


**Fig. 6.** 2D AFM images of thin films with segmentation mask (left images) and texture profiles of thin films (right graphs); (a, a′) P44, (b, b′) P89, (c, c′) P105.

**Table 3**
Fractal parameters of thin films based on AFM images.

| Sample code | Ra [nm] | Rq [nm] | d [nm] | Sk [-] | Ku [-] |
|---|---|---|---|---|---|
| P44 | 1.61 | 1.79 | 36.9 | 0.32 | 2.63 |
| P89 | 1.82 | 2.04 | 35.0 | -0.01 | 3.11 |
| P105 | 2.10 | 2.55 | 46.7 | -0.26 | 3.70 |

**Table 4**
Hardness and toughness parameters of thin films.

| Sample code | H [GPa] | E [GPa] | H/E [-] | $H^3/E^2$ [GPa] | $H/E^2$ [$GPa^{-1}$] |
|---|---|---|---|---|---|
| P44 | 19.3±2.0 | 209.0±9.2 | 0.092 | 0.164 | 0.00044 |
| P89 | 19.9±0.8 | 204.9±4.6 | 0.097 | 0.187 | 0.00047 |
| P105 | 23.1±0.9 | 233.1±6.7 | 0.099 | 0.226 | 0.00042 |

## 4. Discussion

To the best of our knowledge, the effect of thin film morphology on its hardness has not been investigated effectively. Therefore, the top-surface and cross-sectional morphology should be analyzed simultaneously. Because of contact area at the top-surface, the size and shape of surface grains are significant. Hence, according to Hall-Petch theory [71], grain size is inversely proportional to the hardness and toughness of materials. Furthermore, unlike the other study [72], grain size will have an effect on toughness ($H/E^2$) directly and may not always change hardness linearly (see Fig. 12). Based on Fig. 12, in the case of ceramic film toughness, it can be concluded that $H/E^2$ data are more reliable rather than the trends of H, H/E and $H^3/E^2$. In addition, the effect of cross-sectional morphology on hardness is significant. Hardness variation in P44 is high (±2 GPa), which means that various locations have different strengths. It is probably due to its columnar structure, so some dense sites have high strengths but some open boundary sites (as mentioned in previous studies [19,26]) have low strengths. Inversely, the hardness fluctuations of P89 and P105 are lower than 1 GPa because of the dense and featureless structure at the top-surface (like the mechanism discussed in [4] that oxygen incorporation can create an amorph layer at the top-surface of thin films).

As well as morphology, hardness is affected by surface chemistry like bonding structure and defect densities [7,11]. As can be seen from Section 3.1.1., it can be concluded that the origin of the ascending trend of hardness is due to the rising trend of oxygen and carbon content (see Table 2). In the case of oxygen, it can increase configurational entropy (the data obtained by Eq. 2 are presented in Table 6) and hardness is increased by alloying strengthening mechanism [12,43]. As a result, the first sample (P44) shows a W-Ti-C-N thin film, but the others present different chemistry (W-Ti-C-N-O). In the case of carbon, it may be related to the $sp^3$ content in the DLC phase, so some parameters should be brought up. Hence, the $I_D$, G-position (see Fig. 3), $sp^3$ content and residual stress values are listed in Table 6. The FWHM is not used because it shows no clear trend neither in this project nor in the other study [67]. The intensity of the D-shoulder in Raman spectra shows an important enhancement with increasing peak power and carbon content. This increment may be related to structural defects and can enhance hardness. This assumption is well matched with Ref. [32]. Moreover, according to Eq. 4 (where the reference G-position of pure DLC or Pos. G′ is 1568.3 and $\lambda_0$ is 514 nm [56]) [73], shifting the G-position to higher wavenumbers can increase the $sp^3$: $sp^2$ ratio and the bond strength will improve. The calculated $sp^3$ contents in Table 6 confirm this idea. To add to it, residual stress in the sputtering process is of great importance because it influences mechanical properties [39,63]. There is a promising method to measure residual stress in thin films by band position in Raman spectra. On the basis of Eq. 5 (υ is 0.25 [19]) [56], the compressive residual stresses are listed in Table 6 for the samples. It is clear that increasing target power can raise $sp^3$ content and residual stress levels notably (from P89 to P105). Thus, these factors can be the main reasons explaining the extraordinary behavior of the hardness augmentation (from 19.9 to 23.1 GPa). In addition, the Young's modulus of coatings is important because it has two major effects. The first and foremost is that the lower the Young's modulus, the higher the toughness and ductility parameters can gain (toughness of ceramic coatings is defined by H/E, $H^3/E^2$ and $H/E^2$ [10,55,69]). Last but not least is that lower Young's modulus of thin films can reduce the "Ec-Es" parameter (Ec is the Young's modulus of coating and Es is the Young's modulus of substrate/D2 steel-196.1 GPa-) and this can decrease misfit stresses at the substrate-coating interfaces [16]. The

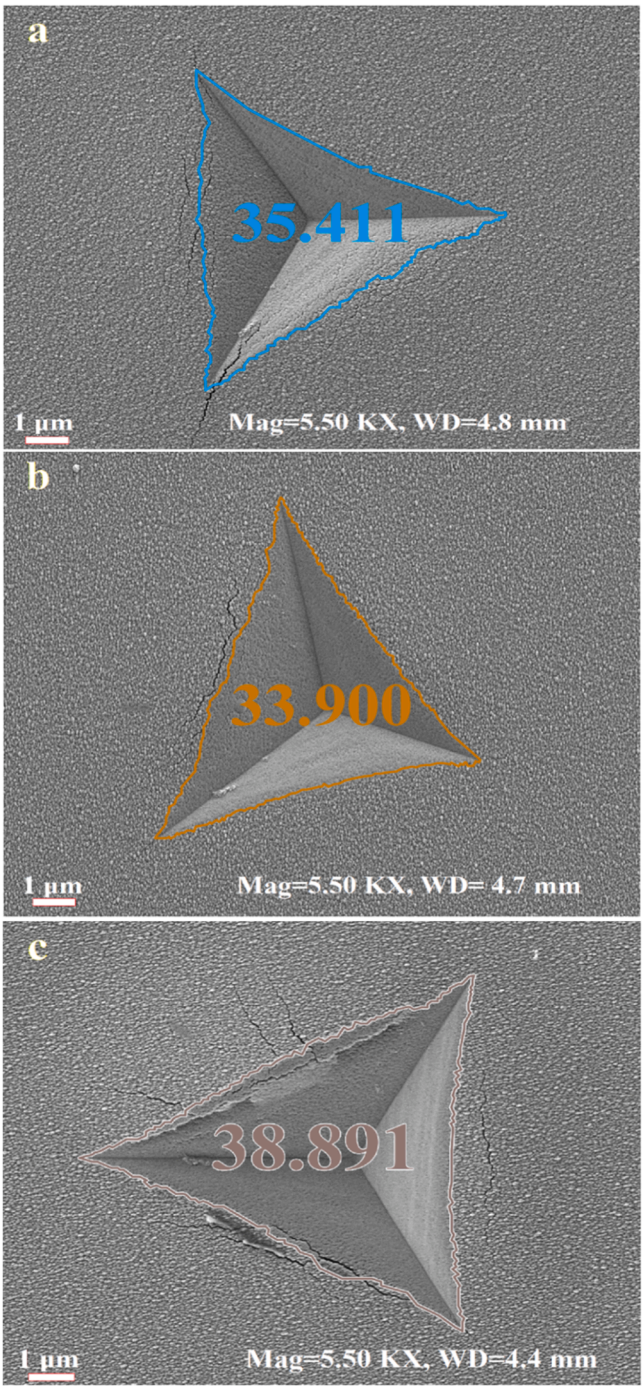


**Fig. 7.** Top-view SEM images of deformation area after 450 mN indentation; (a) P44, (b) P89, (c) P105 (for interpretation of the references to color in this figure legend, the reader is referred to the web version of this article.).

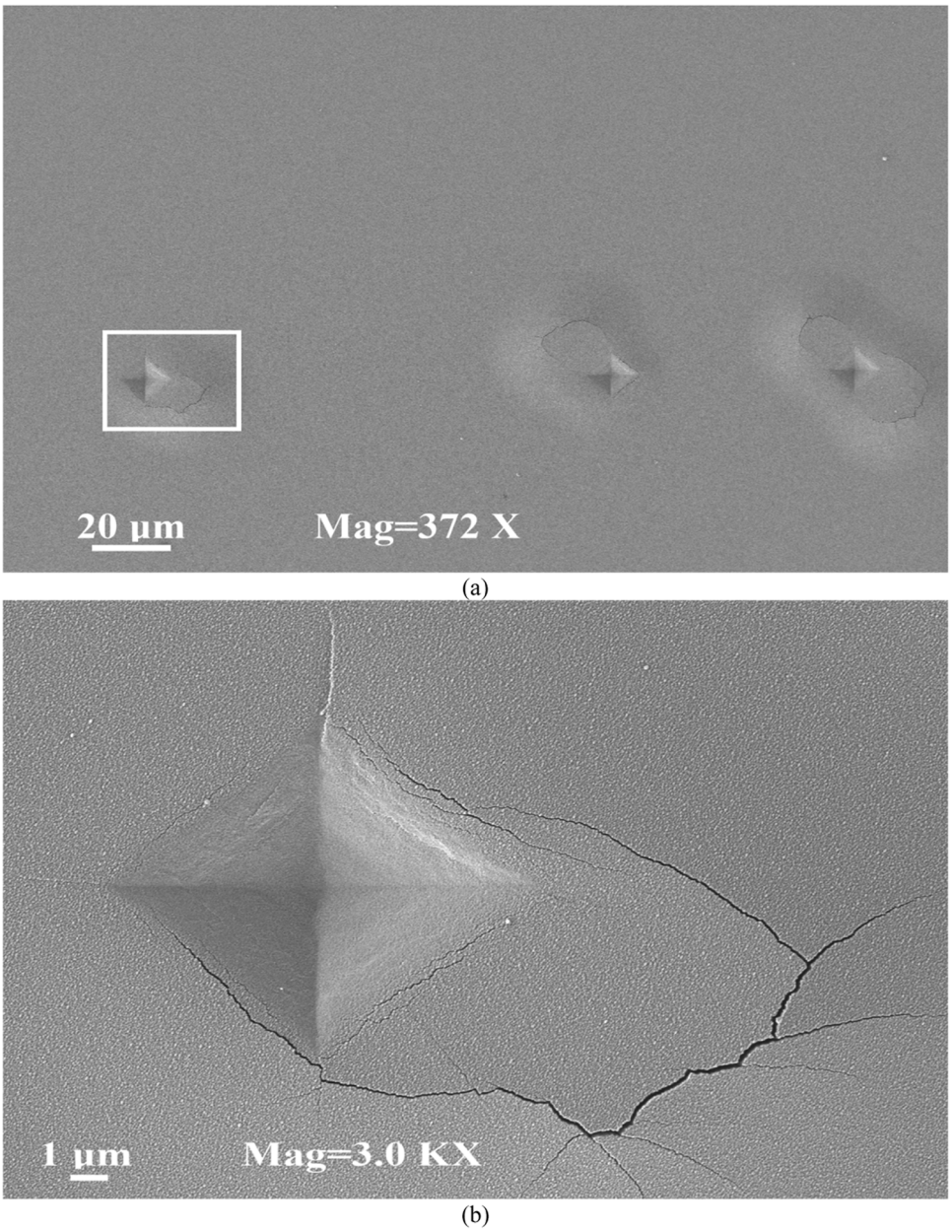


**Fig. 8.** Top-view SEM images of deformation area of sample P105 after 1 N indentation; (a) low magnification (b) high magnification of the white inset in (a).

**Table 5**
Adhesion parameters of thin films.

| Sample code | $L_C1$ [N] | $L_C2$ [N] | CPR [$N^2$] | Shear bands | Crack density | Buckling |
|---|---|---|---|---|---|---|
| P44 | 11.5±3.1 | 25.2±4.6 | 157 | Yes | High | Yes |
| P89 | 23.7±2.2 | 42.6±2.5 | 448 | No | Low | No |
| P105 | 21.4±1.9 | 40.1±2.3 | 400 | Yes | High | Yes |

earlier reason is the main proof for the lowest crack length (collecting crack lengths in each coating based on Fig. 7) and deformation area of sample P89 (see Fig. 13). Employing crack length (like Ref. [74]) and deformation area (like Ref. [75]) is advisable because the equation of fracture toughness ($Kc=\alpha \times E^{0.5} \times H^{-0.5} \times P \times c^{-1.5}$ [54]) is not applicable in this case (coating thickness may have a great effect on results [61] in high load indentations). The trends of crack length and residual deformation area of the coatings are inversely proportional to $H/E^2$ values. This finding shows that the trend of deformation in ceramic films (when the content of C+N + O ≥ 60 at%) does not follow the trend of H, H/E and $H^3/E^2$ parameters (see Table 4), unlike metallic films (∑Mi≥45 at%) [36,46]. The second reason is the major proof of lower substrate-coating adhesion behavior. Because ruptures, shear bands and buckling phenomena in samples P44 and P105 are created substantially (see Figs. 8, 9 and Fig. S6 in the supplementary file). In the case of sample P89, the lowest value of Ec is attributed to the high percentages of oxygen (when nitrogen is replaced by oxygen, the bonding strength gets weaker [76]).

In machining industries, it is necessary to have higher surface uniformity and substrate-coating adhesion. Therefore, lower mass loss and wear rate under service conditions can be achieved [3,40]. Depositing by hybrid sputtering (DCMS and HiPIMS), coatings with uniform and defectless surfaces (no macro-defects were detected) are synthesized. The abovementioned conditions (maximum degree of smoothness and adhesion) are satisfied, provided that the bias voltage and peak power are fixed at the median levels (see the topographic characteristics of P89 in Table 3). In this case, the roughness is lower than 2.04 nm, skewness

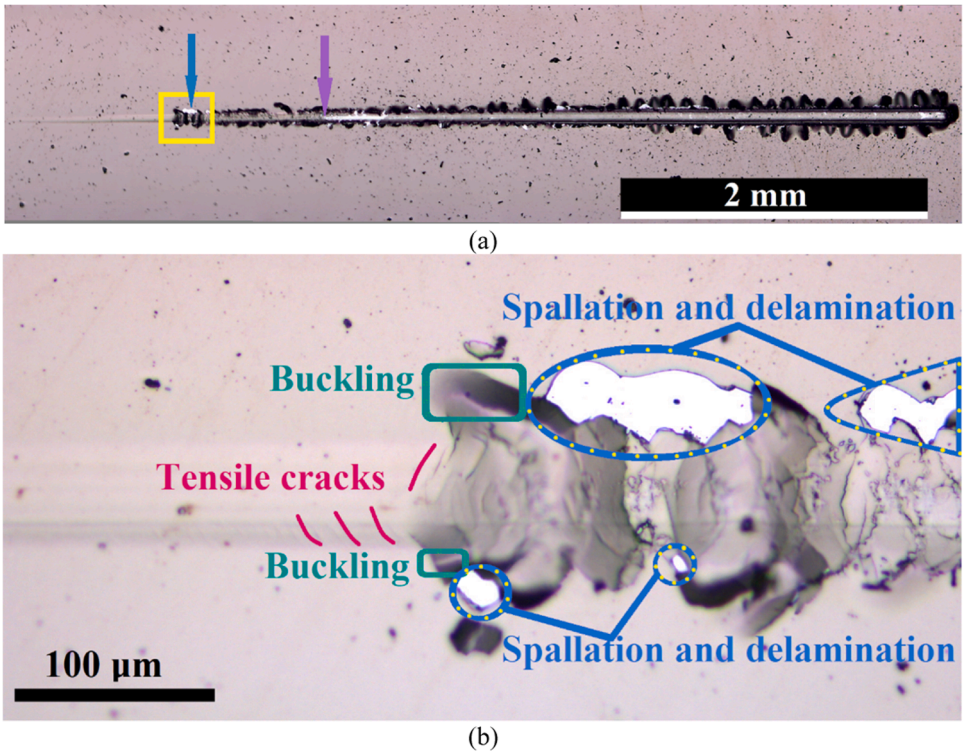


**Fig. 9.** Optical images of deformation area of the first sample-P44- after scratch test; (a)low magnification (b) high magnification of the yellow inset in (a) (for interpretation of the references to color in this figure legend, the reader is referred to the web version of this article.).

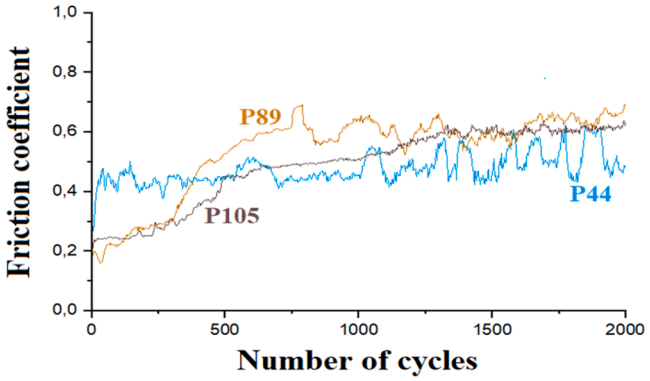


**Fig. 10.** Friction coefficient of thin films based on pin-on-disk tests.

is almost zero and kurtosis is near the value of three. Thus, according to the hypothesis explained in Ref. [59], the surface smoothness of this sample is maximum. In the case of sample P44, the top-surface features are acceptable but its major issue is the columnar nature (see its cross-section image in Fig. 4a). This can facilitate crack propagation [31] and deteriorate mechanical properties significantly. Although the other sample (P105) has a uniform surface (roughness is lower than 2.55 nm, and there is no columnar morphology at the top-surface), the level of Sk and Ku is not desirable. A higher kurtosis (which can create sharp peaks and valleys-see Fig. 6c′-) and negative skewness (which can generate textured grains-see Fig. 6c-) can cause a lower degree of smoothness. These topographical parameters will definitely influence material detachments and wear rate. The columnar character in P44 can cause a high wear rate ($2.7 \times 10^{-5}$ $mm^3$/N.m), while the negative Sk (at a high level) and high Ku in P105 can cause mild wear ($5.9 \times 10^{-6}$ $mm^3$/N.m), and the near zero skewness and kurtosis of 3.1 can cause minimum wear rate ($8.1 \times 10^{-7}$ $mm^3$/N.m). These wear modes are illustrated in Fig. 14, where the green rhomboid shows ultra-mild wear (P89), the orange rhomboid indicates mild wear (P105) and the red rhomboid demonstrates severe wear (P44). In fact, on the basis of sliding test results (scratch and pin-on-disk tests), this figure is a kind of wear map (like the ones defined in Adachi's articles [1,2]) that helps mechanical engineers detect the safe zone. This shows that in order to gain an applicable coating, it is necessary to achieve higher values of CPR as well as minimum wear rate. Because if the CPR of a ceramic film is low, detached ceramic particles (which can be a source to make third bodies) can be located in the wear track and cause more abrasive conditions.

$$\Delta S_{mix} = -R\sum Ci\ Ln\ (Ci) \quad (2)$$

$$Disp{\cdot}(G) = |(Pos{\cdot}G - Pos{\cdot}G')/(\lambda - \lambda_0)| \quad (3)$$

$$sp^3\ content = (-0{\cdot}07 + 2{\cdot}5 \times Disp{\cdot}(G)) \pm 0{\cdot}06 \times 100 \quad (4)$$

$$\sigma = 2\ G \times (1+\upsilon)/(1-\upsilon) \times (Pos{\cdot}G - Pos{\cdot}G')/(Pos{\cdot}G') \quad (5)$$

$$G = E/2(1+\upsilon) \quad (6)$$

Where $\Delta S_{mix}$ is the configurational entropy, R is the gas constant, Ci is the atomic percentage of element "i". In addition, Disp. (G) denotes G-band variation (with dimensions of $cm^{-1}$/nm). E, G and σ (in GPa) indicate the Young's modulus, shear modulus and residual stress of the coatings, respectively.

## 5. Conclusions

Chemical, topographical and mechanical data of W-Ti-C-N(O) thin films have been studied by means of various tests. The composite microstructure (the major phase is amorphous and low amounts of crystalline phases are embedded in this matrix) varies greatly by altering peak power. Therefore, it can be summarized that:

1. Increasing target power in HiPIMS can cause a significant lift of oxygen content in the coatings. Oxygen can be entered into thin films not only as an impurity, but also can be regarded as a principal

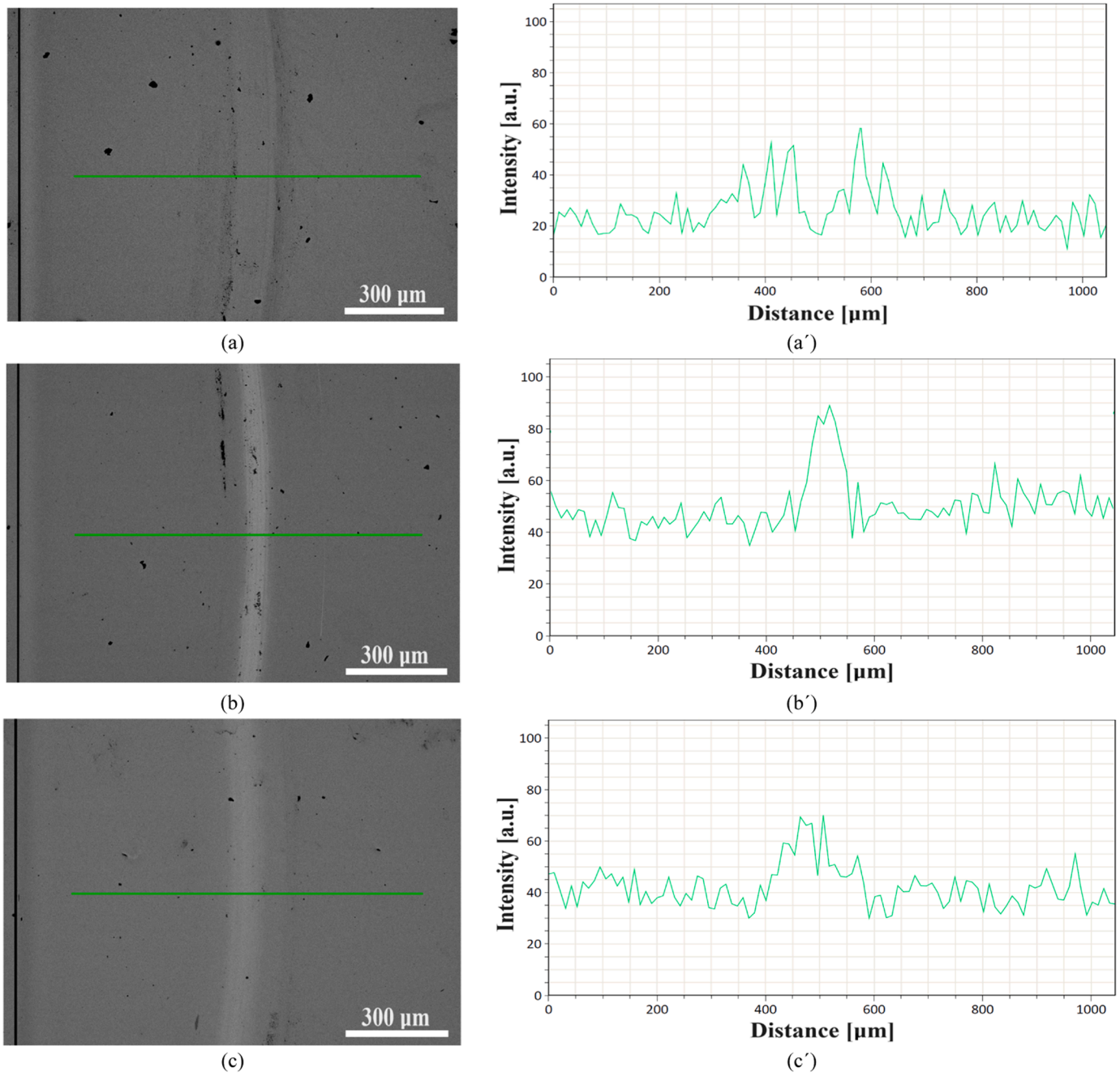


**Fig. 11.** Wear track and oxygen EDS line of thin films; (a, a′) P44, (b, b′) P89, (c, c′) P105.

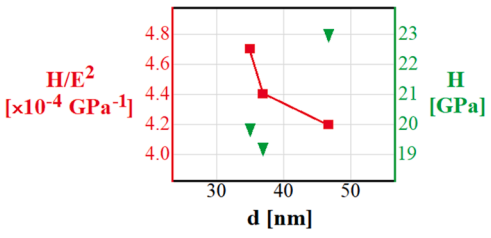


**Fig. 12.** Effect of grain size on hardness and toughness parameter of thin films.

**Table 6**
Hardness and brittleness origins of thin films.

| Sample code | ΔS [J/K. mol] | $I_D$ [a. u.] | Pos. G [$cm^{-1}$] | $sp^3$ content [%] | σ [GPa] | Ec-Es [GPa] |
|---|---|---|---|---|---|---|
| P44 | 1.26 R | 314 | 1581 | 9.8 | -2.3 | 12.9 |
| P89 | 1.51 R | 2063 | 1583 | 12.4 | -2.6 | 8.8 |
| P105 | 1.47 R | 2166 | 1592 | 24.3 | -4.7 | 37 |

element (if O > 8 at%). Hence, this variation can cause a transformation from W-Ti-C-N thin film to W-Ti-C-N-O coatings.

2. Hardness increases with increasing target power. This behavior can be interpreted by higher carbon content, $sp^3$ bond and compressive residual stress content (extracted from Raman spectra).

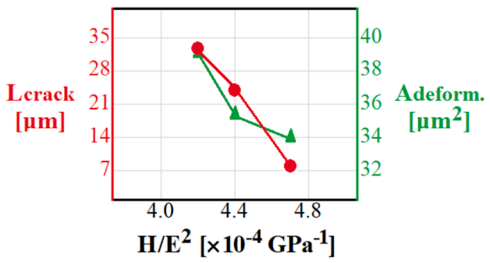


**Fig. 13.** Effect of toughness parameter on fracture and deformation behavior of coatings.

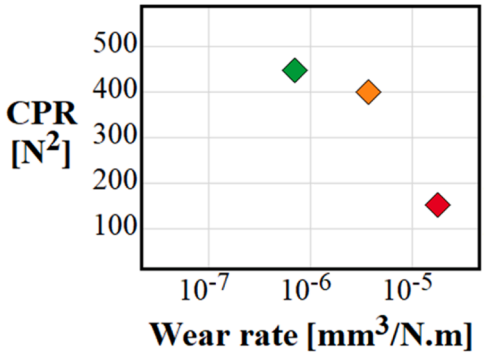


**Fig. 14.** Wear map of thin films based on scratch and pin-on-disk tests; Green color denotes ultra-mild wear, orange color denotes mild wear and red color denotes severe wear (for interpretation of the references to color in this figure legend, the reader is referred to the web version of this article.).

3. The Young's modulus of the coating has a great effect on the toughness ($H/E^2$) and adhesion (Ec-Es). If this parameter increases (as in the values in P44 and P105), then buckling, shear bands and delamination can take place.
4. According to scratch and pin-on-disk results (CPR and wear rate data), a new wear map is introduced to analyze wear modes. It is indicated that not only minimum wear rate is essential but also maximum CPR is vital to gain a desirable coating (P89).

## Declaration of Competing Interest

The authors declare that they have no known competing financial interests or personal relationships that could have appeared to influence the work reported in this paper.

## Data availability

Data will be made available on request.

## Acknowledgement

This research is sponsored by national funds through FCT – Fundação para a Ciência e a Tecnologia, under the project UIDB/00285/2020.

## Appendix A. Supporting information

Supplementary data associated with this article can be found in the online version at doi:10.1016/j.triboint.2023.108983.

## References

[1] Adachi K, Kato K, Chen N. Wear map of ceramics. Wear 1997;203–204:291–301. https://doi.org/10.1016/S0043-1648(96)07363-2.
[2] Adachi K, Hutchings IM. Wear-mode mapping for the micro-scale abrasion test. Wear 2003;255:23–9. https://doi.org/10.1016/S0043-1648(03)00073-5.
[3] Taherkhani K, Soltanieh M. Investigation of nanomechanical and adhesion behavior for AlN coating and AlN/Fe2–3N composite coatings created by Active Screen Plasma Nitriding on Al 1050. J Alloy Compd 2019;783:113–27. https://doi.org/10.1016/j.jallcom.2018.12.282.
[4] Tonshoff K, Karpuschewski B, Mohlfeld A, Leyendecker T, Erkens G, Fuß HG, Wenke R. Performance of oxygen-rich TiAlON coatings in dry cutting applications. Surf Coat Technol 1998;108–109:535–42. https://doi.org/10.1016/S0257-8972(98)00637-9.
[5] Bull SJ. Failure mode maps in the thin film scratch adhesion test. Trib Int 1997;30:491–8. https://doi.org/10.1016/S0301-679X(97)00012-1.
[6] Merl DKek, Panjan P, Panjan M, Čekada M. The role of surface defects density on corrosion resistance of PVD hard coatings. Plasma Process Polym 2007;4:613–7. https://doi.org/10.1002/ppap.200731416.
[7] Veprek S, Veprek-Heijman MGJ, Karvankova P, Prochazka J. Different approaches to superhard coatings and nanocomposites. Thin Solid Films 2005;476:1–29. https://doi.org/10.1016/J.TSF.2004.10.053.
[8] Cheng Z, Wang S, Wu G, Gao J, Yang X, Wu H. Tribological properties of high-entropy alloys: a review. Int J Min Metal Mater 2022;29:389. https://doi.org/10.1007/s12613-021-2373-4.
[9] Zhang N, Klippel H, Afrasiabi M, Röthlin M, Kuffa M, Bambach M, Wegener K. Hybrid SPH-FEM solver for metal cutting simulations on the GPU including thermal contact modeling. CIRP J Man Sci Technol 2023;41:311–27. https://doi.org/10.1016/j.cirpj.2022.12.012.
[10] Smolik J, Sowa S, Kacprzynska-Gołacka J, Piasek A. Evaluation of the fracture toughness KIc for selected magnetron sputtering coatings by using the Laugier model. Materials 2022;15:9061. https://doi.org/10.3390/ma15249061.
[11] ZHANG Y, ZHANG Z, WANG X, YAO W, LIANG X. Structure and properties of high-entropy amorphous thin films: a review. JOM 2022;74. https://doi.org/10.1007/s11837-021-05107-w.
[12] Glatz SA, Bolvardi H, Kolozsvári S, Koller CM, Riedl H, Mayrhofer PH. Arc evaporated W-alloyed Ti-Al-N coatings for improved thermal stability, mechanical, and tribological properties. Surf Coat Technol 2017;332:275–82. https://doi.org/10.1016/j.surfcoat.2017.05.097.
[13] Huang X, Sun S, Tu G. Investigation of mechanical properties and oxidation resistance of CVD $TiB_2$ ceramic coating on molybdenum. J Mater Res Technol 2020;9:282–90. https://doi.org/10.1016/j.jmrt.2019.10.056.
[14] Gassner M, Rebelo de Figueiredo M, Schalk N, Franz R, Weiß C, Rudigier H, Holzschuh H, Bürgin W, Pohler M, Czettl C, Mitterer C. Energy consumption and material fluxes in hard coating deposition processes. Surf Coat Technol 2016;299:49–55. https://doi.org/10.1016/j.surfcoat.2016.04.062.
[15] Raghavan R, Wheeler JM, los Ojos DE, Thomas K, Almandoz E, Fuentes GG, Michler J. Mechanical behavior of Cu/TiN multilayers at ambient and elevated temperatures: Stress-assisted diffusion of Cu. Mater Sci Eng A 2014;620:375–82. https://doi.org/10.1016/j.msea.2014.10.023.
[16] Shtanskii DV, Kulinich SA, Levashov EA, Moore JJ. Structure and physical-mechanical properties of nanostructured thin films. Phys Solid State 2003;45:1177–84. https://doi.org/10.1134/1.1583811.
[17] Wani SM, Ahmad B, Saleem SS. Nano-mechanical and nano-tribological characterization of Ni-Co-BN nano-composite coating for bearing applications. Trib Int 2023;180:108281. https://doi.org/10.1016/j.triboint.2023.108281.
[18] Ding Z, Tang Y, Liu L, Ding Z, Tan Y, He Q. Improving the adhesive, mechanical, tribological properties and corrosion resistance of reactive sputtered tantalum oxide coating on Ti6Al4V alloy via introducing multiple interlayers. Ceram Int 2022;48:5983–94. https://doi.org/10.1016/j.ceramint.2021.11.134.
[19] Ataie SA, Soltanieh M, Naghizadeh R, Ahmadi M, Ghanaatshoar M. Effects of substrate temperature and reactive gas flow rate on the crystalline ceramic phases formation and tribological properties of W–Ti–Co–C–N thin films produced by co-sputtering. Ceram Int 2020;46:29137–49. https://doi.org/10.1016/j.ceramint.2020.08.087.
[20] Liew WY Hsien, Lim HP, Melvin GJ Hong, Dayou J, Jiang Z. Thermal stability, mechanical properties, and tribological performance of TiAlXN coatings: understanding the effects of alloying additions. J Mater Res Technol 2022;17:961–1012. https://doi.org/10.1016/j.jmrt.2022.01.005.
[21] Gudmundsson JT. The high power impulse magnetron sputtering discharge as an ionized physical vapor deposition tool. Vacuum 2010;84:1360–4. https://doi.org/10.1016/j.vacuum.2009.12.022.
[22] Emmerlich J, Mraz S, Snyders R, Jiang K, Schneider JM. The physical reason for the apparently low deposition rate during high-power pulsed magnetron sputtering. Vacuum 2008;82:867–70. https://doi.org/10.1016/j.vacuum.2007.10.011.
[23] Sarakinos K, Alami J, Konstantinidis S. High power pulsed magnetron sputtering: a review on scientific and engineering state of the art. Surf Coat Technol 2010;204:1661–84. https://doi.org/10.1016/j.surfcoat.2009.11.013.
[24] Torrisi V, Ruffino F. Nanoscale structure of submicron-thick sputter-deposited Pd films: effect of the adatoms diffusivity by the film-substrate interaction. Surf Coat Technol 2017;315:123–9. https://doi.org/10.1016/j.surfcoat.2017.02.034.
[25] Bakhit B, Mraz S, Lu J, Rosen J, Schneider JM, Hultman L, Petrov I, Greczynski G. Dense Ti0.67Hf0.33B1.7 thin films grown by hybrid HfB2-HiPIMS/TiB2-DCMS co-sputtering without external heating. Vacuum 2021;186:110057. https://doi.org/10.1016/j.vacuum.2021.110057.
[26] Bakhit B, Dorri S, Kosari A, Mol A, Petrov I, Birch J, Hultman L, Greczynski G. Microstructure, mechanical, and corrosion properties of Zr1-xCrxBy diboride alloy thin films grown by hybrid high power impulse/DC magnetron co-sputtering. Appl Surf Sci 2022;591:153164. https://doi.org/10.1016/j.apsusc.2022.153164.
[27] Gui B, Zhou H, Zheng J, Liu X, Feng X, Zhang Y, Yang L. Microstructure and properties of TiAlCrN ceramic coatings deposited by hybrid HiPIMS/DC magnetron

co-sputtering. Ceram Int 2021;47:8175–83. https://doi.org/10.1016/j.ceramint.2020.11.175.
[28] Ataie SA, Keshtmand R, Zamani-Meymian MR. Nano-mechanical properties of Cr-Zr-Nb-N medium entropy alloy films produced by reactive sputtering. Int J Ref Met Hard Mat 2023;110:106006. https://doi.org/10.1016/j.ijrmhm.2022.106006.
[29] Ferreira F, Cavaleiro A, Oliveira JC. Effect of substrate biasing on the structure and properties of tantalum coatings deposited using HIPIMS in deep oscillation magnetron sputtering mode. Metals 2020;10:1618. https://doi.org/10.3390/met10121618.
[30] Ferreira F, Oliveira JC, Cavaleiro A. CrN thin films deposited by HiPIMS in DOMS mode. Surf Coat Technol 2016;291:365–75. https://doi.org/10.1016/j.surfcoat.2016.02.064.
[31] Ataie SA, Soltanieh M, Naghizadeh R, Cavaleiro A, Evaristo M, Fernandes F, Ferreira F. Effect of substrate bias voltage on structural and tribological properties of W-Ti-C-N thin films produced by combinational HiPIMS and DCMS co-sputtering. Wear 2023:204654. https://doi.org/10.1016/j.wear.2023.204654.
[32] Mashoff T, Convertino D, Miseikis V, Coletti C, Tozzini V, Beltram F, Heun S. increasing the active surface of titanium islands on graphene by nitrogen sputtering. Appl Phys Lett 2015;106:083901. https://doi.org/10.1063/1.4913562.
[33] Zhao J, Liu Z, Wang B, Song Q, Ren X, Wan Y. Effects of Al content in TiAlN coatings on tool wear and cutting temperature during dry machining IN718. Trib Int 2022;171:107540. https://doi.org/10.1016/j.triboint.2022.107540.
[34] Nouvellon C, Belchi R, Libralesso L, Douhéret O, Lazzaroni R, Snyders R, Thiry D. WC/C:H films synthesized by an hybrid reactive magnetron sputtering/plasma enhanced chemical vapor deposition process: an alternative to Cr (VI) based hard chromium plating. Thin Solid Films 2016. https://doi.org/10.1016/j.tsf.2016.09.002.
[35] Ren Y, Niu Y, Jia J, Cao X, Zhang G. Design and tribological performance of CrN/Mo2N/MoSx composite coating in wide temperature range inspired by oxidation kinetics principle. Trib Int 2023;180:108229. https://doi.org/10.1016/j.triboint.2023.108229.
[36] Zhao H, Ni Z, Ye F. Effect of carbon content on structure and properties of WCN coatings prepared by RF magnetron sputtering. Surf Coat Technol 2016;287:129–37. https://doi.org/10.1016/j.surfcoat.2016.01.003.
[37] Ding Z, Wang Y, Zhou Q, Ding Z, Wu Y, Zhu Y, Shi W, He Q. The preparation and properties of multilayer Cu-MTa2O5 composite coatings on Ti6Al4V for biomedical applications. Nanomaterials 2019;9:1498. https://doi.org/10.3390/nano9101498.
[38] Addonizio ML, Castaldo A, Antonaia A, Gambale E, Iemmo L. Influence of process parameters on properties of reactively sputtered tungsten nitride thin films. J Vac Sci Technol A 2012;30:031506. https://doi.org/10.1116/1.3698399.
[39] Mishra AK, Gopalan H, Hans M, Kirchlechner C, Schneider JM, Dehm G, Jaya BN. Strategies for damage tolerance enhancement in metal/ceramic thin films: Lessons learned from Ti/TiN. Acta Mater 2022;228:117777. https://doi.org/10.1016/j.actamat.2022.117777.
[40] Larhlimi H, Ghailane A, Makha M, Alami J. Magnetron sputtered titanium carbide-based coatings: a review of science and technology. Vacuum 2022;197:110853. https://doi.org/10.1016/j.vacuum.2021.110853.
[41] Shang X, Liu Q, Guo Y, Ding K, Liao T, Wang F. Nano-TiC reinforced [Cr–Fe4Co4Ni4]Cr3 high-entropy-alloy composite coating fabricated by laser cladding. J Mater Res Technol 2022;21:2076–88. https://doi.org/10.1016/j.jmrt.2022.10.048.
[42] Yoon JS, Myung HS, Han JG, Musil J. A study on the synthesis and microstructure of WC-TiN superlattice coating. Surf Coat Technol 2000;131:372–7. https://doi.org/10.1016/S0257-8972(00)00808-2.
[43] Vieira MT, Cavaleiro A, Trindade B. The effects of a third element on structure and properties of W-C/N. Surf Coat Technol 2002;151–152:495–504. https://doi.org/10.1016/S0257-8972(01)01640-1.
[44] Cavaleiro A, Trindade B, Vieira MT. Influence of Ti addition on the properties of W–Ti-C/N sputtered films. Surf Coat Technol 2003;174 –175:68–75. https://doi.org/10.1016/S02578972(03)00328-1.
[45] Gaedike B, Guth S, Kern F, Killinger A, Gadow R. Deposition of 3YSZ-TiC PVD coatings with high-power impulse magnetron sputtering (HiPIMS). Appl Sci 2021;11:2753. https://doi.org/10.3390/app11062753.
[46] Lyu L, Yang J, Zhou M, Yan M, Yang J. Microstructure, mechanical properties and lead-bismuth eutectic corrosion behavior of (AlCrFeTiMo)NO and (AlCrFeTiNb)NO high entropy metal sublattice ceramic coatings. Vacuum 2023;209:111774. https://doi.org/10.1016/j.vacuum.2022.111774.
[47] Hsieh JH, Wu W, Li C, Yu CH, Tan BH. Deposition and characterization of Ti (C, N, O) coatings by unbalanced magnetron sputtering. Surf Coat Technol 2003;163–164:233–7. https://doi.org/10.1016/S0257-8972(02)00494-2.
[48] Olteanu C, Munteanu D, Ionescu C, Munteanu A, Chappé JM, Cunha L, Vaz F. Tribological characterisation of magnetron sputtered Ti (C, O, N) thin films. Int J Mater Prod Technol 2010;39. https://doi.org/10.1504/IJMPT.2010.034270.
[49] Stanishevsky A, Lappalainen R. Tribological properties of composite Ti (N, O, C) coatings containing hard amorphous carbon layers. Surf Coat Technol 2000;123:101–5. https://doi.org/10.1016/S0257-8972(99)00514-9.
[50] Shtansky DV, Levashov EA, Glushankova NA, D'yakonova NB, Kulinich SA, Petrzhik MI, Kiryukhantsev-Korneev FV, Rossi F. Structure and properties of CaO- and ZrO2-doped TiCxNy coatings for biomedical applications. Surf Coat Technol 2004;182:101–11. https://doi.org/10.1016/S0257-8972(03)00813-2.
[51] Aliramaji S, Keuter P, Neuß D, Hans M, Primetzhofer D, Depla D, Schneider JM. Effect of growth temperature and atmosphere exposure time on impurity incorporation in sputtered Mg, Al, and Ca thin films. Materials 2023;16:414. https://doi.org/10.3390/ma16010414.
[52] Greczynski G, Mraz S, Hultman L, Schneider JM. Venting temperature determines surface chemistry of magnetron sputtered TiN films. Appl Phys Lett 2016;108:041603. https://doi.org/10.1063/1.4940974.
[53] Volinsky AA, Moody NR, Gerberich WW. Interfacial toughness measurements for thin films on substrates. Acta Mater 2002;50:441–66. https://doi.org/10.1016/S1359-6454(01)00354-8.
[54] Zhang S, Sun D, Fu Y, Du H. Toughness measurement of thin films: a critical review. Surf Coat Technol 2005;198:74–84. https://doi.org/10.1016/j.surfcoat.2004.10.021.
[55] Musil J, Jirout M. Toughness of hard nanostructured ceramic thin films. Surf Coat Technol 2007;201:5148–52. https://doi.org/10.1016/j.surfcoat.2006.07.020.
[56] Wei Q, Sharma AK, Sankar J, Narayan J. Mechanical properties of diamond-like carbon composite thin films prepared by pulsed laser deposition. Compos: Part B 1999;30:675–84. https://doi.org/10.1016/S1359-8368(99)00035-9.
[57] Sung SL, Guo XJ, Huang KP, Chen FR, Shih HC. The strengthening mechanism of DLC film on silicon by MPECVD. Thin Solid Films 1998;315:345–50. https://doi.org/10.1016/S0040-6090(97)00782-7.
[58] Koski K, Holsa J, Juliet P. Surface defects and arc generation in reactive magnetron sputtering of aluminium oxide thin films. Surf Coat Technol 1999;115:163–71. https://doi.org/10.1016/S0257-8972(99)00172-3.
[59] Kotwal CA, Bhushan B. Contact analysis of non-gaussian surfaces for minimum static and kinetic friction and wear. Trib Trans 1996;39:890–8. https://doi.org/10.1080/10402009608983609.
[60] Pharr GM, Oliver WC. Measurement of thin film mechanical properties using nanoindentation. MRS Bull 1992;17:28–33. https://doi.org/10.1557/S0883769400041634.
[61] Anstis GR, Chantikul P, Lawn BR, Marshall DB. A critical evaluation of indentation techniques for measuring fracture toughness: i, direct crack measurement. J Am Ceram Soc 1981:533–8. https://doi.org/10.1111/j.1151-2916.1981.tb10320.x.
[62] Constable CP, Yarwood J, Münz WD. Raman microscopic studies of PVD hard coatings. Surf Coat Technol 1999;116–119:155–9. https://doi.org/10.1016/S0257-8972(99)00072-9.
[63] Constable CP, Lewis DB, Yarwood J, Munz WD. Raman microscopic studies of residual and applied stress in PVD hard ceramic coatings and correlation with X-ray diffraction (XRD) measurements. Surf Coat Technol 2004;184:291–7. https://doi.org/10.1016/j.surfcoat.2003.10.014.
[64] Yoshikawa M, Katagiri G, Ishida H, Ishitani A, Akamatsu T. Raman spectra of diamondlike amorphous carbon films. J Appl Phys 1988;64. https://doi.org/10.1063/1.342063.
[65] Sharifahmadian O, Pakseresht A, Mirzaei S, Eliáš M, Galusek D. Mechanically robust hydrophobic fluorine-doped diamond-like carbon film on glass substrate. Diam Relat Mater 2023;138:110252. https://doi.org/10.1016/j.diamond.2023.110252.
[66] Zhang S, Yan M, Yang Y, Zhang Y, Yan F, Li H. Excellent mechanical, tribological and anti-corrosive performance of novel Ti-DLC nanocomposite thin films prepared via magnetron sputtering method. Carbon 2019;151:136e147. https://doi.org/10.1016/j.carbon.2019.05.031.
[67] Choi J, Ishii K, Kato T, Kawaguch M, Lee W. Structural and mechanical properties of DLC films prepared by bipolar PBII&D. Diam Relat Mater 2011;20:845–8. https://doi.org/10.1016/j.diamond.2011.04.003.
[68] Anders A, Andersson J, Ehiasarian A. High power impulse magnetron sputtering: current-voltagetime characteristics indicate the onset of sustained self-sputtering. J Appl Phys 2007;102:113303. https://doi.org/10.1063/1.2817812.
[69] Pintaude G. Introduction of the Ratio of the Hardness to the Reduced Elastic Modulus for Abrasion, Tribology - Fundamentals and Advancements. IntechOpen; 2013. https://doi.org/10.5772/55470.
[70] Joslin DL, Oliver WC. A new method for analyzing data from continuous depth-sensing microindentation tests. J Mater Res 1990;5. https://doi.org/10.1557/JMR.1990.0123.
[71] Armstrong RW. Hall-Petch analysis of dislocation pileups in thin material layers and in nanopolycrystals. J Mat Res Soc 2013;28:1792–8. https://doi.org/10.1557/jmr.2013.10.
[72] HAHN H, PADMANABHAN KA. A model for the deformation of nanocrystalline materials. Philos Mag B 1997;76:559–71. https://doi.org/10.1080/01418639708241122.
[73] Thiry D, De Vreese A, Renaux F, Colaux JL, Lucas S, Guinet Y, Paccou L, Bousser E, Snyders R. Toward a better understanding of the influence of the hydrocarbon precursor on the mechanical properties of a-C:H coatings synthesized by a hybrid PECVD/PVD method. Plasma Process Polym 2016;13:316–23. https://doi.org/10.1002/ppap.201500050.
[74] Yang C, Yao Y, Huan Y, Fu Z, Chen F, Lavernia EJ. Tough TiB2-based ceramic composites using metallic glass powder as the sintering aid. Adv Eng Mater 2016. https://doi.org/10.1002/adem.201600234.
[75] Xie T, Zhu J, Fu L, Zhang R, Li N, Yang M, Wang J, Qin W, Yang W, Li D, Zhou L. The evolution of hardness in Cu-W alloy thin films. Mater Sci Eng A 2018;729:170–7. https://doi.org/10.1016/j.msea.2018.05.035.
[76] Hans M, to Baben M, Music D, Ebenhöch J, Primetzhofer D, Kurapov D, Arndt M, Rudigier H, Schneider JM. Effect of oxygen incorporation on the structure and elasticity of Ti-Al-O-N coatings synthesized by cathodic arc and high power pulsed magnetron sputtering. J Appl Phys 2014;116:093515. https://doi.org/10.1063/1.4894776.